A Bayesian statistical approach to inferring particle dynamics from in-situ pump POC and chloropigment data from the Mediterranean Sea

Wei-Lei Wang[a,*], Cindy Lee[b], François W. Primeau[a]

[a] Department of Earth System Science, University of California at Irvine, Irvine, USA
[b] School of Marine and Atmospheric Sciences, Stony Brook University, Stony Brook, NY 11790-5000, USA

ABSTRACT

Concentrations of chloropigments and particulate organic carbon (POC) in large-volume in-situ pump samples from the Mediterranean Sea were used to estimate rate constants of processes that control the fate of particles, and specifically chloropigments, in the water column. Here we introduce a Bayesian statistical inversion method that combines the data with a new box model and has the capacity to infer rate constants for POC respiration/dissolution, chlorophyll and pheopigment degradation, and particle aggregation and disaggregation. We use first-order kinetics to model disaggregation, and use both first-order and second-order kinetics to model aggregation. Using these methods, the estimated small-particle (1–70 μm) POC respiration rate constant was $2.44^{+1.69}_{-1.00}$ yr^{-1} (0.41 yr). The estimated disaggregation and second-order aggregation rate constants were $85.6^{+63.4}_{-36.4}$ yr^{-1} (1.17×10^{-2} yr) and $2.78^{+2.01}_{-1.17}$ μM^{-1} yr^{-1}, respectively. Using the optimal rate constants and the corresponding particle concentrations, disaggregation is ~4.2 times faster than the small-size POC dissolution rate, which indicates that disaggregation is a dominant processes at the time of sampling. More importantly, by comparing our results with those of previous studies, we conclude that sampling methods have less influence than tracers themselves on inferring particle dynamic rate constants. We previously introduced a somewhat similar approach to modeling SV sediment trap data, but large volume pumps are a much more common sample collection method in oceanographic surveys than SV sediment traps, and thus our new model should have a wider applicability.

1. Introduction

Sinking particles transport organic carbon to the ocean interior at a globally significant rate of 4–14 Pg C yr^{-1} (Lima et al. 2014; Emerson 2014), and this is one of the few natural processes removing CO_2 from the atmosphere for periods significant to climate change. However, most organic matter produced by photosynthesis in the euphotic zone, a key source of marine particles, is consumed or respired in the upper ocean. Less than 10% of the total organic matter produced there is transported into the deep ocean by sinking particles (Lee and Wakeham 1988). Theoretically, particle density and size determine particle sinking speed according to Stokes' law, and thus residence time in the water column (McCave 1975; Clegg and Whitfield 1991; Armstrong et al. 2002). However, processes such as aggregation and disaggregation can alter this relationship and ultimately influence particle transfer efficiency (e.g. McDonnell and Buesseler 2010).

Historically, the quantitative dynamics of particle aggregation and disaggregation processes has been studied using thorium isotopes (e.g. Bacon and Anderson 1982; Clegg and Whitfield 1991; Clegg et al. 1991; Murnane 1994; Murnane et al. 1996; Cochran et al. 1993; Cochran et al. 2000), and much of what we currently know about the dynamics of these processes is from work with particulate thorium. Thorium radioisotopes have unique advantages, e.g., multiple radionuclides can share the same chemical characteristics but have different decay half-lives, which offers independent constraints on particle fluxes. In addition, the environmental sources of these radionuclides are well-known. However, thorium tracers also suffer from several inherent disadvantages: 1) different particle components have different degrees of affinity to thorium (Roy-Barman et al. 2005); 2) the particulate thorium activity of short-lived isotopes (e.g. ^{234}Th) become very low (below detection limits) in the oligotrophic deep ocean, which can limit their applicability; and 3) dissolved ^{234}Th activity is orders of magnitude higher than particulate activity, thus in models, dissolved thorium influences the adsorption-desorption balance more than particulate thorium does, making the disaggregation rate constant very sensitive to small errors in the adsorption rate constant, as illustrated by Wang et al.

---

* Corresponding author.
 E-mail address: weilei.wang@gmail.com (W.-L. Wang).

(2016). To make this last point clear, assuming first-order reaction kinetics and steady state, an activity balance of small-size particulate ^{234}Th can be expressed using the following equation:

$$\kappa_1 [Th_d] - (\kappa_{-1} + \alpha + \lambda_{234})[Th_s] + \beta [Th_l] = 0, \qquad (1)$$

where κ_1, κ_{-1}, α, β, and λ_{234} are adsorption, desorption, aggregation, disaggregation, and ^{234}Th radioactivity decay constants, respectively. $[Th_d]$, $[Th_s]$, and $[Th_l]$ are dissolved, small- and large-size particulate ^{234}Th activities, respectively. Typical dissolved and large-size particulate ^{234}Th activities in the surface ocean are 2400 and 2 dpm m^{-3}, respectively. A small change in adsorption rate constant κ_1 (e.g. $\delta\kappa_1 = 0.1$) changes the disaggregation rate constant by a factor of 120, if we assume other processes are unchanged. Below we document the advantages and disadvantages of chloropigments relative to those of thorium. The use of multiple tracers should provide a more complete picture of particle dynamics in the ocean than the use of thorium or chloropigment tracers alone.

Chlorophyll *a* (Chl *a*) is an essential pigment that is produced during phytoplankton photosynthesis. Chloropigment (Chl *a* and its degradation products: pheophorbide, pyropheophorbide, and pheophytin) tracers were first proposed as an alternative for thorium isotopes in tracing particle dynamics by Wang et al. (2017), who used chloropigments sampled using Indented Rotating Sphere (IRS) sinking velocity (SV) traps to study particle aggregation and disaggregation. In that study, particle sinking speeds were measured using SV traps, and sinking particles were grouped into two categories based on their sinking speed. A two-layer model was applied to estimate particle aggregation and disaggregation, and particulate organic matter respiration rate constants. Compared to thorium as a tracer, one distinct advantage of chloropigments is that they do not adsorb to or desorb from particles. Chloropigments are also an integral part of most marine particles formed in the euphotic zone. Wang et al. (2017) compared aggregation and disaggregation rate constants obtained using chloropigment concentrations to their counterparts obtained using thorium isotope activities. In that case, chloropigment concentrations and thorium activities were measured in samples from the same sediment trap. There were clear differences in the results from the two different tracers: aggregation and disaggregation rate constants estimated from chloropigments were orders of magnitude higher than those from thorium tracers, indicating that due to the distinctly different properties of the two tracers, they trace particle processes differently. One should note that making inferences about particle dynamics is complicated because different sampling methods in addition to different tracers have the potential to influence our conclusions. Therefore, this paper aims to investigate how the choice of sampling methods versus tracers affects our inferences.

SV sediment traps have a major advantage compared to other techniques, such as time-series sediment traps or large volume pumps, because SV sediment traps can measure both sinking particle flux and particle sinking velocity (Peterson et al. 2005, 2009; Armstrong et al. 2009). By using SV trap data, we can avoid any assumptions that link particle size to particle sinking velocity, assumptions that may not be true in the ocean (e.g., McDonnell and Buesseler 2010). However, due to the lack of easy commercial availability, SV sediment traps have not been widely used in oceanographic surveys. In addition, interpretation of aggregation and disaggregation derived from SV traps seems ambiguous, since traditionally it is thought that aggregation is the process of small particles colliding with other particles and becoming larger, and disaggregation is the process of larger particles breaking up into smaller particles. However, particles in fast sinking categories are a combination of large and small particles, because some smaller particles have higher sinking speed, and vice versa (McDonnell and Buesseler 2010).

In-situ pumps can collect both large and small particles by filtering the seawater through filters or meshes of different size (e.g., Bishop et al. 2012). In terms of flux measurements, these pumps have a drawback in that they take a snapshot of the water column only over a 1–2 day period and the different depths are not always sampled on the same day due to logistical constraints. In addition, particles can break up on filters and may not reflect their in-situ size. However, they are much cheaper than traps, have simpler electronics, and are easier to deploy and recover. Unfortunately, there has been no generally accepted method to convert pump-derived concentrations to flux.

If both sinking flux and sinking velocity are known, a conceptual model is relatively easy to build (Wang et al. 2017). However, in-situ particle sinking velocity is rarely measured, thus, different techniques are required to model pigment concentrations sampled using large-volume pumps at multiple depths. In the following, chloropigments sampled using large-volume pumps were used to study particle aggregation, disaggregation, and particulate organic carbon respiration rate constants. The objectives of this new work were 1) to introduce a new method that allows us to study particle dynamics using chloropigment (or other geochemical tracer) concentrations measured in samples from large volume pumps, 2) to compare particle exchange rate constants with two other studies at the same site, and 3) to determine whether the tracer used or the sampling technique used is a more important constraint on modeled rate constants. This third goal was particularly interesting to us. Wang et al. (2016) and Wang et al. (2017) used the same sampling techniques but different tracers (thorium and chloropigments, respectively). The present study and (Wang et al. 2017) used the same chloropigment tracers but sampled using different techniques, i.e. SV trap versus large volume pumps. The intercomparisons we describe here allow us to investigate whether sampling techniques (pumps vs traps) or the tracer itself (chloropigments vs thorium) imposed the stronger constraint on modeled rate constants.

2. Methods

2.1. Sampling site

Samples were collected using in-situ pumps as part of the MedFlux project at the French JGOFS DYFAMED (Dynamics of Atmospheric Fluxes in the Mediterranean) site (43°20′N, 7°40′E) in the Mediterranean Sea in May 2005 (Cochran et al. 2009). Lee et al. (2009a) describe the DYFAMED site and why it was chosen for the MedFlux study. This site in the Ligurian Sea has an average water depth of 2300 m and is 53 km from the coast at Nice. It is traditionally treated as an open ocean site because the longshore Ligurian current cuts off most terrestrial influence (Marty et al. 2002). This site is characterized by strong winter mixing and low winter primary production, followed by a strong phytoplankton spring bloom from March to April. The spring bloom is terminated by summer stratification and thus a shorter supply of nutrients. A smaller phytoplankton bloom in fall is promoted by the decrease in stratification at that time.

2.2. Sampling and analyses

MedFlux chloropigment and POC sampling methods, analytical procedures, and pump concentration data have been described and discussed previously in Abramson et al. (2010). Essentially, large volume in-situ pumps (Challenger Oceanic) were used to collect particle samples that were separated into two groups based on their size. Seawater flowed first through a 70-μm Nitex screen that retained larger ($> 70\,\mu$m) particles, and then through a 1-μm quartz microfiber filter that retained smaller (1–70 μm) particles. Once retrieved, half of each 142-mm filter was frozen for later chloropigment analyses. Material collected on the 70-μm filter is typically thought to be more representative of sinking particulate matter, whereas material passing through the larger filter and collected on the 1-μm filter is typically thought to be a more slowly settling fraction (Cochran and Masqué 2003). As discussed in Abramson et al. (2010), if Stokes' law were applied to these particles, the 70-μm cutoff would be roughly equivalent

Table 1

Concentrations in μM of data collected using large volume pumps at the MedFlux/DYFAMED Site (43°20′N, 7°40′E) in the Mediterranean Sea in May 2005 [Cochran et al. (2009)]. The left-side columns are for small particles (S) (1–70 μm). The rest are for large particles (> 70 μm) (L). According to [Abramson et al. 2010], replicate pigment samples (i.e., duplicate punches taken from different places on the same pump filter) generally differed within 30% (calculated by propagation of error). POC data have much lower uncertainty (2%). The corresponding measurement errors are incorporated in data covariance matrix (Σ_d).

Site	Depth	Chl a(S)	POC(S)	Σ(Pheo)(S)	Chl a(L)	POC(L)	Σ(Pheo)(L)
	(m)	(μM)	(μM)	(μM)	(μM)	(μM)	(μM)
D	100	1.30×10^{-5}	1.89	3.32×10^{-5}	1.76×10^{-8}	2.32×10^{-1}	2.34×10^{-7}
Y	125	9.35×10^{-6}	1.26	1.49×10^{-5}	1.63×10^{-8}	1.02×10^{-1}	1.01×10^{-7}
F	150	6.21×10^{-6}	1.04	6.52×10^{-6}	1.98×10^{-8}	8.23×10^{-2}	1.41×10^{-7}
A	200	2.63×10^{-6}	0.64	6.60×10^{-6}	3.13×10^{-8}	1.56×10^{-1}	1.15×10^{-7}
M	300	1.37×10^{-6}	0.44	1.88×10^{-6}	1.22×10^{-8}	4.15×10^{-2}	8.91×10^{-8}
E	500	1.54×10^{-6}	0.44	1.81×10^{-6}	1.36×10^{-8}	8.12×10^{-2}	1.22×10^{-7}
D	750	3.75×10^{-7}	0.51	1.12×10^{-6}	3.43×10^{-9}	6.44×10^{-2}	6.41×10^{-8}

Σ(Pheo) means Σ(pheophorbide, pyropheophorbide, pheophytin).

to a division between particles settling at speeds less (slowly sinking) and more (faster sinking) than 0.5 m d^{-1}.

2.3. Data selection

The original data used in our model are shown in Table 1. The MedFlux site was surveyed during multiple cruises in 2003 and 2005; however, only data from pump samples collected in late May 2005 are used in this study, because > 70-μm-size particles were only collected at that time. Samples in the euphotic zone (depth < 80 m) and below the nepheloid layer (depth > 2000 m) were excluded to reflect only the export zone and to eliminate the influences of primary production and sediment resuspension.

According to our CTD data, the mixed layer at the time of pump sampling was 20–30 m (Lee et al. 2009b). In addition, more extensive studies of the mixed layer at this location (e.g. D'Ortenzio et al. 2005; Houpert et al. 2015) show that the mixed layer depth at this location is always less than ~ 50 m, which is well above our studied depths. A more detailed description of these and other MedFlux chloropigment data, both in general terms and in a discussion of qualitative evidence for aggregation and disaggregation, can be found in Abramson et al. (2010).

2.4. Conceptual models

We modified the conceptual model used in Wang et al. (2017) for sediment trap particles to tailor it for pump data (Fig. 1). Specifically, we model smaller and larger particle groups rather than slow- and fast-sinking particle groups. The description of the conceptual model is similar to our previous model. For example, small and large particles exchange particle components via aggregation and disaggregation: larger particles disaggregate to form smaller particles, and smaller particles aggregate to become larger particles. Chl a that originates in small phytoplankton is incorporated into larger particles via aggregation, and pheopigments that are products of zooplankton digestion can be associated with smaller particles via particle disaggregation (Abramson et al. 2010). In addition, some pheopigments are products of microbial Chl-a degradation, and can therefore be produced directly in small particles. Small-size POC and pheopigments can be respired to CO$_2$. Chl a also can degrade to colorless components, disappearing from our analytical window. However, current analytical methods did not allow us to distinguish this latter pathway. Future quantification of colorless product formation will allow inclusion of this pathway in the model. However, here we ignore this process as did in Wang et al. (2017).

2.5. Mathematical descriptions

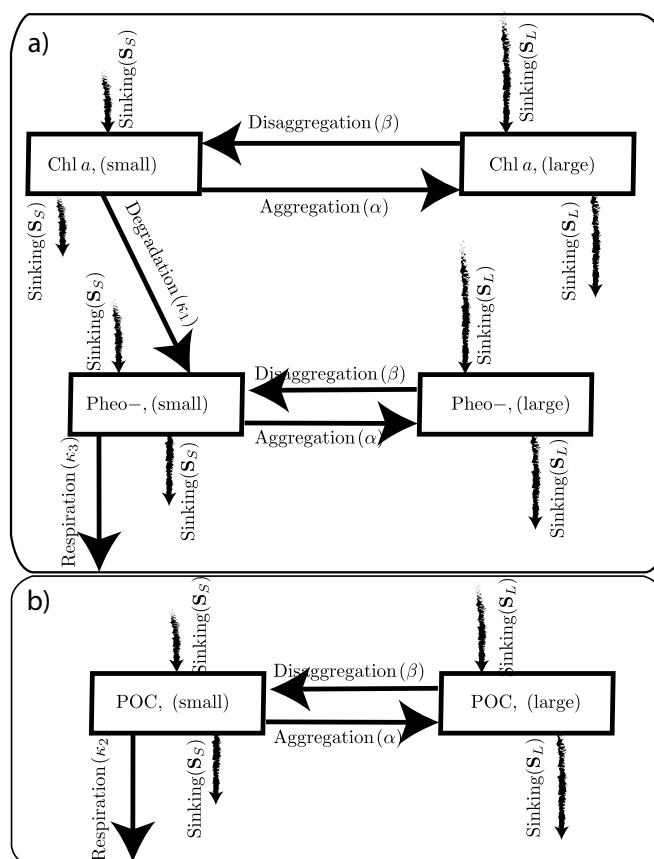We assume first-order reaction kinetics for disaggregation since

Fig. 1. Conceptual model modified from that in Wang et al. (2017) for particle fluxes. One significant difference is that for the pumps, we used small and large size particles instead of slow- and fast-sinking particles. In addition, aggregation and disaggregation occur between small and large particles, instead of between slow- and fast- sinking particles as in Wang et al. (2017). Both small- and large-size particles sink in the water column.

disaggregation is the breakdown of a large particle into smaller particles, and a linear dependence on concentration is a reasonable assumption. However, aggregation kinetics are more complicated because aggregation usually involves two or more particles, and particles need to collide to aggregate. To simplify mathematical models, first-order kinetics has been widely used in previous thorium-based studies (e.g. Murnane et al. 1990; Cochran et al. 1993; Marchal and Lam 2012). However, Jackson (1990) and Jackson and Burd (2015) argue that aggregation is a non-linear process, with an aggregation kernel that depends on particle sinking speed, stickiness, and size. To reconcile the

differences, we first model aggregation using second-order reaction kinetics (Eqs. 2–7). We ignore aggregation between small and large particles since concentrations of large particles are 2–3 orders of magnitude lower than that of small particles (Table 1), and thus their interaction rates are assumed to be low. We then compare the first- and second-order reaction aggregation models to 1) determine how different kinetics can influence our results, and 2) facilitate the comparisons with previous results, which are based on steady-state and first-order aggregation assumptions.

For large size POC, we have the following governing equation:

$$\frac{d[\mathbf{POC_L}]}{dt} = \underbrace{\alpha[\mathbf{POC_S}][\mathbf{POC_S}]}_{Aggregation} - \underbrace{\beta[\mathbf{POC_L}]}_{Disaggregation} - \underbrace{\mathbf{S_L}[\mathbf{POC_L}]}_{Sinking} + [\mathbf{POC_L}]_x,$$

(2)

and for small size POC, we have the following governing equation:

$$\frac{d[\mathbf{POC_S}]}{dt} = \underbrace{\beta[\mathbf{POC_L}]}_{Disaggregation} - \underbrace{\kappa_2[\mathbf{POC_S}]}_{Respiration} - \underbrace{\alpha[\mathbf{POC_S}][\mathbf{POC_S}]}_{Aggregation} - \underbrace{\mathbf{S_S}[\mathbf{POC_S}]}_{Sinking}$$
$$+ [\mathbf{POC_S}]_x,$$

(3)

where α and β are aggregation and disaggregation rate constants, respectively. κ_2 is the small-sized POC dissolution rate constant. The bold variables (e.g. $[\mathbf{POC_L}]$ and $[\mathbf{POC_S}]$) represent 7×1 vectors, for the concentrations at each discrete depth level. The subscripts L and S denote large- and small-size POC, respectively. The downward tracer transport by sinking particles is modeled using a transport operator, $\mathbf{S}$, which is constructed from a powerlaw flux attenuation profile according to Martin et al. (1987). Given an assumed constant particle dissolution rate and an exponent 'b' one can define a particle sinking speed (ω) that reproduces the powerlaw flux attenuation profile (Kriest and Oschlies (2008). Since the large particle dissolution rate is not modeled, we used a disaggregation rate constant as a substitute. The resulting particle flux divergence, $\frac{\partial(\omega c)}{\partial z}$, can be written as a matrix vector product in which the elements of the vector $\mathbf{c}$ are the particle concentrations in a set of discrete layers and the matrix, $\mathbf{S}$, is constructed using finite-differences and a discretized vector of sinking velocities, $\mathbf{w}$, defined at the interfaces separating the layers. For example, if we divide the water column into 7 layers, the concentration of a tracer can be organized into the vector, $\mathbf{c}$, and the discretized flux divergence is given by $\mathbf{Sc}$ where $\mathbf{S}$ is a 7×7 matrix. We neglect advective and diffusive transport of particles because their influence is assumed to be small compared to other source and sink terms (Savoye et al. 2006). $[\mathbf{POC}_{L/S}]_x$ (or similarly $[\mathbf{Chl}_{L/S}]_x$ and $[\mathbf{Phy}_{L/S}]_x$ in Eqs. 4 and 7, respectively) is the source of POC that sinks out of the euphotic zone and into the model's uppermost box.

Chl a is assumed to originate only in smaller particles. This is a reasonable assumption considering the sampling time (May 2005). At that time, the spring bloom is already over, and diatom density should be low so that primary production should be dominated by smaller phytoplankton (Marty et al. 2002). Table 1 shows that Chl-a concentrations were very low at the sampling time, indicating a low primary production condition. Then we assume that any Chl a found in large particles is from small particle aggregation. We also assume that Chl a has a two-step degradation: it first degrades to pheopigments, which then further degrade to CO_2. The governing equations for pigments are as follow.

$$\frac{d[\mathbf{Chl_L}]}{dt} = \underbrace{\alpha[\mathbf{Chl_S}][\mathbf{Chl_S}]}_{Aggregation} - \underbrace{\beta[\mathbf{Chl_L}]}_{Disaggregation} - \underbrace{\mathbf{S_L}[\mathbf{Chl_L}]}_{Sinking} + [\mathbf{Chl_L}]_x,$$

(4)

$$\frac{d[\mathbf{Chl_S}]}{dt} = \underbrace{\beta[\mathbf{Chl_L}]}_{Disaggregation} - \underbrace{\kappa_1[\mathbf{Chl_S}]}_{Degradation} - \underbrace{\alpha[\mathbf{Chl_S}][\mathbf{Chl_S}]}_{Aggregation} - \underbrace{\mathbf{S_S}[\mathbf{Chl_S}]}_{Sinking}$$
$$+ [\mathbf{Chl_S}]_x,$$

(5)

$$\frac{d[\mathbf{Phy_L}]}{dt} = \underbrace{\alpha[\mathbf{Phy_S}][\mathbf{Phy_S}]}_{Aggregation} - \underbrace{\beta[\mathbf{Phy_L}]}_{Disaggregation} - \underbrace{\mathbf{S}[\mathbf{Phy_L}]}_{Sinking} + [\mathbf{Phy_L}]_x,$$

(6)

$$\frac{d[\mathbf{Phy_s}]}{dt} = \underbrace{\beta[\mathbf{Phy_l}]}_{Disaggregation} + \underbrace{\kappa_1[\mathbf{Chl_s}]}_{Degradation} - \underbrace{\kappa_3[\mathbf{Phy_s}]}_{Degradation} - \underbrace{\alpha[\mathbf{Phy_s}][\mathbf{Phy_s}]}_{Aggregation}$$
$$- \underbrace{\mathbf{S_S}[\mathbf{Phy_S}]}_{Sinking} + [\mathbf{Phy_S}]_x,$$

(7)

where κ_1 is the rate constant for degradation of Chl a to pheopigments, and κ_3 is the pheopigment respiration rate constant.

2.5.1. Steady state model

Since we do not have time-series measurements, we have no way to build a traditional non-steady state model. Instead we first assume the system is at steady state, but we nevertheless take into account the impact of non-steady state behavior on our inferences (see section 2.5.2). At steady state, we ignore the time derivative terms ($d()/dt$) on the left hand side of Eq. 2 through Eq. 7. And the resulting discretized equations can be written as a system of 42 equations with 42 unknowns (6 tracers in 7 discrete layers). In vector form we have

$$\mathbf{F}(\mathbf{x}) = 0,$$

(8)

where $\mathbf{F}$ is a 42×1 non-linear function where ($\mathbf{x^T} = [\mathbf{POC_l}, \mathbf{POC_s}, \mathbf{Chl_l}, \mathbf{Chl_s}, \mathbf{Phy_l}, \mathbf{Phy_s}]$), that is, a 1×42 row vector. The non-linearity is due to second-order reaction kinetics for aggregation. We solve the equation using Newton's method.

$\mathbf{F}$ is also a function of $k = 13$ unknown parameters, $[b_L, b_S, \alpha, \beta, \kappa_1, \kappa_2, \kappa_3, [\mathbf{POC_L}]_x, [\mathbf{Chl_L}]_x, [\mathbf{Phy_L}]_x, [\mathbf{POC_S}]_x, [\mathbf{Chl_S}]_x, [\mathbf{Phy_S}]_x]$, which makes the solution $\mathbf{x}$ an implicit function of these parameters. (Note that b is the powerlaw exponent used to formulate the sinking particle transport operator, ($\mathbf{S}$).) We estimate these parameters using a two-level Bayesian process. At the first level we estimate the vector of parameters, e.g., ($\mathbf{p} = \log [b_L, b_S, \alpha, \beta, \kappa_1, \kappa_2, \kappa_3, [\mathbf{POC_L}]_x, [\mathbf{Chl_L}]_x, [\mathbf{Phy_L}]_x, [\mathbf{POC_S}]_x, [\mathbf{Chl_S}]_x, [\mathbf{Phy_S}]_x]$) by assigning a normal probability distribution to the prior probability for $\mathbf{p}$ as well as to the deviations of $\mathbf{x}(\mathbf{p})$ from the observations. The resulting logarithm of the posterior is given by $-0.5 f(\mathbf{p}|\Gamma, \Lambda) + constant$, with

$$f(\mathbf{p}|\Gamma, \Lambda) = \Gamma(\mathbf{x}(\mathbf{p}) - \mathbf{c_0})'\Sigma_\mathbf{d}^{-1}(\mathbf{x}(\mathbf{p}) - \mathbf{c_0}) + \Lambda(\mathbf{p} - \mathbf{p_0})'\Sigma_\mathbf{p}^{-1}(\mathbf{p} - \mathbf{p_0})$$
$$+ constant,$$

(9)

where $\mathbf{c_0}$ is a vector that contains observed data, and $\mathbf{p_0}$ is a vector that contains the mean of prior probability distribution of the parameters. $\Sigma_\mathbf{d}/\Gamma$ and $\Sigma_\mathbf{p}/\Lambda$ are the covariance matrices for the likelihood and the prior. The hyper-parameters, Γ and Λ scale the data and prior precisions. The relative sizes of Γ and Λ control the relative importance of the prior and the likelihood function in determining the location of the maximum of the posterior probability for the parameters. Their overall magnitude influences the size of the posterior error bars. At the first level, we find the most probable parameter values (conditioned on assumed values for Γ and Λ) by minimizing f using a trust-region algorithm as implemented in Matlab's fminunc function. By optimizing the logarithm of the parameters rather than the parameters themselves we avoid the possibility that the optimization routine will propose negative rate constants. After conditioning on the model, the errors are expected to be independent so that $\Sigma_\mathbf{d}$ is a diagonal matrix, whose diagonal elements are the squares of the measurement standard deviations of the corresponding data. The hyper parameter, Γ, rescales these variances to account for the fact that model errors can also contribute to the misfits. We also assign a diagonal matrix to $\Sigma_\mathbf{p}$, which is equivalent to assuming that a priori knowledge of one parameter does not provide any information on the value of another parameter. We assigned a large prior variance for each parameter (Table 2) to allow the data to have as much influence as possible. Ultimately, only the relative size of the prior parameter precisions matters because we rescale the prior covariance

Table 2
Particle aggregation, disaggregation, chloropigment degradation, and POC dissolution rate constants and $\pm 1\sigma$ errorbars estimated based on pump data sampled at the MedFlux/DYFAMED site (unit: yr^{-1} except for Martin curve exponential b that is dimensionless and second-order aggregation rate constant (α) that has a unit of $\mu\text{M}^{-1}\,\text{yr}^{-1}$). $\exp(\mathbf{p_0})$ is parameter prior, and σ_p^2 is variance. SS and NSS denote steady state and non-steady state results. The last column is reference.

	kinetics	SS/NSS	b_S	b_L	κ_1	κ_2	κ_3	α	β	Ref.
$\exp(\mathbf{p_0})$	–	–	0.87	0.87	1.38	1.38	1.38	5.47	148	
σ_p^2	–	–	0.16	0.16	2.98	2.98	2.98	4.01	6.64	
Pump pigments	2nd-order	NSS1	$0.90^{+0.09}_{-0.08}$	$0.89^{+0.09}_{-0.08}$	$1.38^{+0.75}_{-0.49}$	$1.94^{+0.70}_{-0.52}$	$1.39^{+0.75}_{-0.49}$	$4.84^{+1.69}_{-1.25}$	$144.9^{+66.1}_{-45.4}$	[Ref.]3
Pump pigments	2nd-order	NSS2	$1.00^{+0.22}_{-0.18}$	$0.81^{+0.17}_{-0.14}$	$1.69^{+1.81}_{-1.03}$	$2.46^{+1.77}_{-0.87}$	$2.07^{+1.93}_{-1.00}$	$2.75^{+2.04}_{-1.17}$	$84.6^{+63.7}_{-36.3}$	[Ref.]3
Pump pigments	2nd-order	SS	$0.98^{+0.21}_{-0.17}$	$0.83^{+0.17}_{-0.14}$	$1.68^{+1.74}_{-0.86}$	$2.44^{+1.69}_{-1.00}$	$2.06^{+1.86}_{-0.98}$	$2.78^{+2.01}_{-1.17}$	$85.6^{+63.4}_{-36.4}$	[Ref.]3
Pump pigments	1st-order	SS	$0.93^{+0.24}_{-0.19}$	$0.86^{+0.22}_{-0.18}$	$2.00^{+3.03}_{-1.21}$	$2.66^{+2.49}_{-1.28}$	$1.86^{+2.68}_{-1.10}$	$3.18^{+3.05}_{-1.56}$	$73.1^{+69.6}_{-35.6}$	[Ref.]3
SV Thorium	1st-order	SS	–	–	–	–	–	0.07–1.88	0.30–3.01	[Ref.]4
SV pigment	1st-order	SS	–	–	$1.6^{+0.4}_{-0.3}$	$1.5^{+0.5}_{-0.4}$	$2.1^{+0.7}_{-0.5}$	$3.2^{+9.9}_{-2.4}$	$149.9^{+297.3}_{-99.6}$	[Ref.]5

[1]Corresponding to $\Theta = 10^{-2}$ (see text).
[2]Corresponding to $\Theta = 10^{13}$ (see text).
[3]this study;
[4]Wang et al. (2016);
[5]Wang et al. (2017).

matrix with the hyper parameter, Λ. The trust-region optimization algorithm iteratively searches for optimal parameters. It is very efficient because we are able to provide the gradient and Hessian matrix for $f(\mathbf{p}|\Gamma,\Lambda)$. Typically, we obtain the optimal parameters in less than 50 iterations.

At the second level we estimate Γ and Λ by maximizing Bayesian evidence (MacKay 1992),

$$Z(\Gamma,\Lambda) = \int d\mathbf{p}\,\text{prob}(\mathbf{p}\mid\mathbf{c_{l0}}), \tag{10}$$

which is equivalent to maximizing the likelihood for Γ and Λ. A good approximation to the logarithm of the evidence is given by

$$\log(Z(\Gamma,\Lambda)) = -f(\hat{\mathbf{p}}) - \frac{1}{2}\log(\det(\mathbf{A})) + \frac{k}{2}\log(\Lambda) + \frac{N}{2}\log(\Gamma)$$
$$+ \text{constant}. \tag{11}$$

where $\hat{\mathbf{p}}$ is the vector of optimal parameter values estimated at the first level for a prescribed Γ and Λ. $\mathbf{A}$ is the $k \times k$ Hessian matrix computed by taking the second derivatives of $f(\mathbf{p}|\Gamma,\Lambda)$ given in Eq. 9 with respect to the $k = 13$ parameters and evaluating the resulting 13×13 matrix at the optimal parameter values. Because the first level optimization for $\hat{\mathbf{p}}$ is very fast, we perform the second level optimization by evaluating $\log(Z(\Gamma,\Lambda))$ on a two-dimensional mesh and choosing the arguments, $(\hat{\Gamma}, \hat{\Lambda})$ that yield the maximum (Fig. 2a, c). The two-level evidence maximization algorithm allows for the automatic calibration of the relative importance of the likelihood and prior for the determination of the posterior probability for the parameters, which is then used to find the most probable parameter values along with their errorbars. Our best estimate for each parameter is given by the $\hat{\mathbf{p}}$ that maximizes $f(\mathbf{p}\mid\hat{\Gamma},\hat{\Lambda})$. The parameter errorbars corresponding to $\pm 1\,\sigma$ are determined using Laplaces approximation (e.g. Teng et al. 2014).

2.5.2. Non-steady state model
The validity of the steady-state assumption is somewhat dubious. Phytoplankton blooms at the MedFlux study site evolve with a timescale of a week or so, which does not seem long enough for the full particle flux dynamics to reach steady-state. We therefore wish to test the robustness of our inferences to departures from steady-state. If we allow arbitrary departures from steady-state our biogeochemistry model is able to fit our dataset – which provides only a snapshot view of the particles – with essentially any choice of parameters because the residuals between the steady-state solution and the observations can simply be attributed to the time tendency term. With such a flexible model it is impossible to learn anything about the parameters controlling the particle-flux dynamics.

To make progress we apply an analysis method first developed in Wang et al. (2019) to test the robustness of inverse-model inferences to

the steady-state assumption when the constraining dataset consists of a single snapshot in time. This involves decomposing the model's dynamics into a part that equilibrates quickly on a timescale shorter than that of a bloom, $\tau_{\text{bloom}} \sim 1$ week, and a part that equilibrates more slowly on timescales $\tau > \tau_{\text{bloom}}$. We then allow for departures from steady-state only in the slowly equilibrating dynamical modes.

The decomposition into fast and slowly equilibrating dynamics is achieved through an eigenmode analysis of the linearized model about its steady-state solution at the optimal (steady-state) parameter set, $\mathbf{x}_o(\hat{\mathbf{p}})$. Assuming that such departures are small, the leading-order governing equations for the departures from steady-state, $\mathbf{x}'(t) \equiv \mathbf{x}(t) - \mathbf{x}_o$, can be expressed as

$$\frac{d\mathbf{x}'}{dt} = \mathbf{J}\mathbf{x}', \tag{12}$$

where

$$\mathbf{J} = \left[\frac{\partial \mathbf{F}(\mathbf{x})}{\partial \mathbf{x}}\right]_{\mathbf{x}=\mathbf{x}_o} \tag{13}$$

is the model's Jacobian matrix. The above system of differential equations admits solutions of the form

$$\mathbf{x}'(t) = \sum_{k=1}^{N} a_k \mathbf{v}_k e^{-\sigma_k t}, \tag{14}$$

where $\{\sigma_k, \mathbf{v}_k | k = 1, \cdots, N = 42\}$ are eigenvalue-eigenvector pairs satisfying $-\sigma_k\mathbf{v}_k = \mathbf{J}\mathbf{v_k}$. The real part of the eigenvalues yields the corresponding eigenmode's damping rate and can be used to separate the solution into a weakly damped part with e-folding decay timescales, τ_k's $\equiv 1/\Re\{\sigma_k\} \geq \tau_{\text{bloom}}$ and a strongly damped part with τ_k's $< \tau_{\text{bloom}}$. The a_k's are undetermined amplitudes that can be determined by knowing the solution at some given time. Since the dimensions of the model's state space is equal to the number of amplitudes, any initial condition can be accommodated if we retain all the eigenmodes. Instead we assume that all the strongly damped modes have negligible amplitudes on the grounds that the amplitudes of these modes cannot deviate far from zero before being damped out. The remaining amplitudes corresponding to slowly decaying modes are retained in the model and their unknown amplitudes are added to the list of adjustable parameters, which when marginalized out of the posterior probability will yield errorbars on the other parameters that take into account the possibility that the system is out of equilibrium on longer timescales. Through this procedure we relax the steady state assumption without making the model so flexible that it can teach us nothing about the particle-flux dynamics.
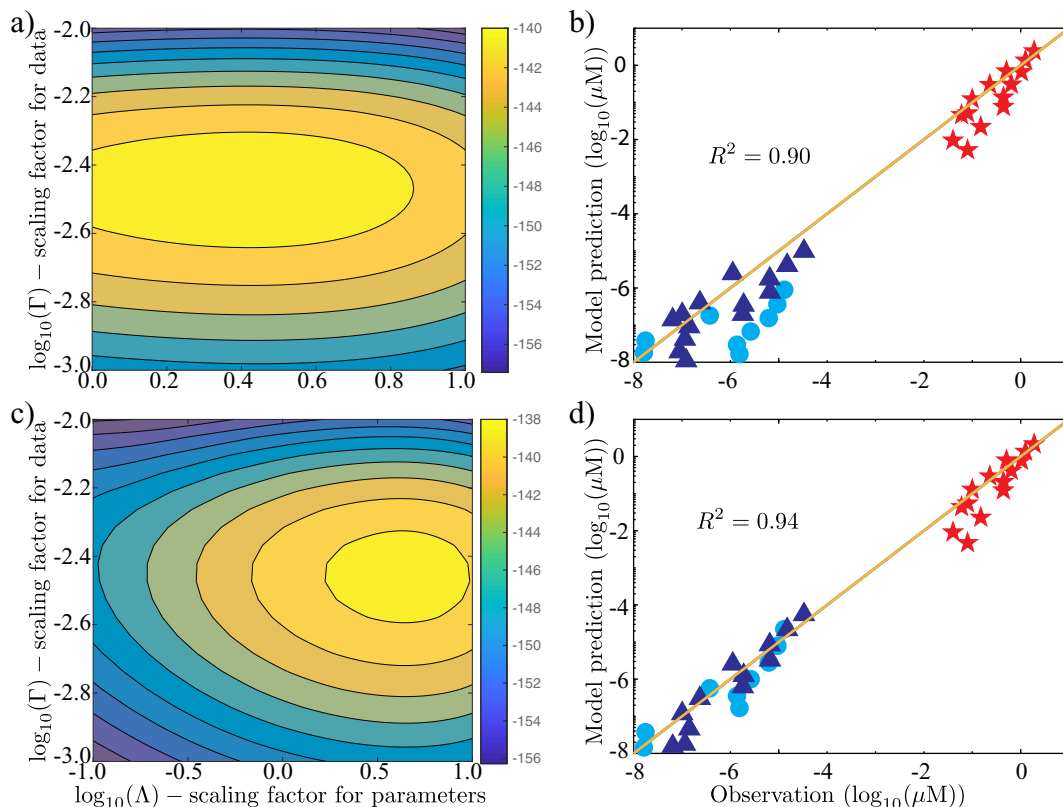
Fig. 2. a) and b) Contour plots of the logarithm of the evidence along with model versus observation comparisons for first-order steady-state model. c) and d) are corresponding plots for the second-order steady-state model. Red stars represent POC, blue triangles correspond to pheopigments, and cyan circles stand for Chl *a*. (For interpretation of the references to colour in this figure legend, the reader is referred to the web version of this article.)

2.5.3. First-order aggregation model

To compare with previous models, in which steady-state and first-order reaction kinetics are assumed for aggregation, we altered Eqs. 2–7 by changing the formulation for aggregation from $\underbrace{\alpha\,[\mathbf{Chl_s}][\mathbf{Chl_s}]}_{Aggregation}$ to $\underbrace{\alpha\,[\mathbf{Chl_s}]}_{Aggregation}$. And then Eqs. 2–7 are simplified into a linear system, which can be easily solved using a direct matrix inversion in Matlab. We then use the same Bayesian inversion method as introduced above to estimate the parameters.

3. Results and discussion

A Bayesian inverse method was previously applied to MedFlux IRS SV sediment trap data to estimate particle exchange parameters (Wang et al. 2017). In that study, the method was tested by creating a set of synthetic data using a finite difference model with a set of known "true" parameters, and then contaminating the data with random errors, finally recovering the "true" parameters by using the inverse method. The same mathematical model is applied here; however, instead of using the two-layer model created to describe data collected using SV sediment traps, we use a box model to describe the data collected using large volume pumps, a sample collection method that is more common in oceanographic surveys than SV sediment traps.

One important difference between pump and SV sediment trap data is that pumps measure concentrations, and SV sediment traps measure particle fluxes at different sinking velocities. The previous "two-layer model" is tailored for flux data because flux differences between trap depths are known. In addition, because the data are available at only three trap depths, they are inadequate to build a traditional box model (Wang et al. 2016, 2017). In contrast, the pump data is available at 7 depths and enables us to create a box model, for which the boundary

condition is estimated as part of the inversion.

3.1. First-order versus second-order model

Fig. 2b and Fig. 2d show model versus observation comparisons for first- and second-order aggregation models, respectively. With the same number of parameters, the second-order model ($R^2 = 0.94$) fits the observations better than the first-order model ($R^2 = 0.90$). However, the estimated values of the common parameters (Table 2) are not significantly different (Note that the aggregation rate constants have different units and are therefore not comparable.). The comparisons here are interesting in several respects. On one hand, the assumptions we made about first- and second-order reaction kinetics of aggregation do not significantly influence POC dissolution and chloropigment degradation rate constant estimates. We think this is mainly due to the fact that aggregation is assumed to occur among particles that have the same size, same stickiness, and are non-sinking, instead of among different classes of particles. On the other hand, the better fit of the second-order model to observed data shows that a second-order model can better represent particle dynamics as suggested by Jackson (1990) and Jackson and Burd (2015).

3.2. Steady state versus non-steady state

Carrying out the eigenmode analysis described in Section 2.5.2 for our model we found 21 modes with *e*-folding decay timescales greater than $\tau_{bloom} = 5$ days (Fig. 3a). The amplitude of these modes were then added to the list of adjustable parameter, $[\mathbf{p}, \mathbf{a}]$, which is now a 34×1 vector (the 13 original model parameters plus 21 amplitudes). With 34 parameters and 36 equations, the system is nearly underdetermined. We thus added a Gaussian prior with zero mean on the amplitudes of the weakly damped eigenmodes with one more hyper-parameter, Θ,
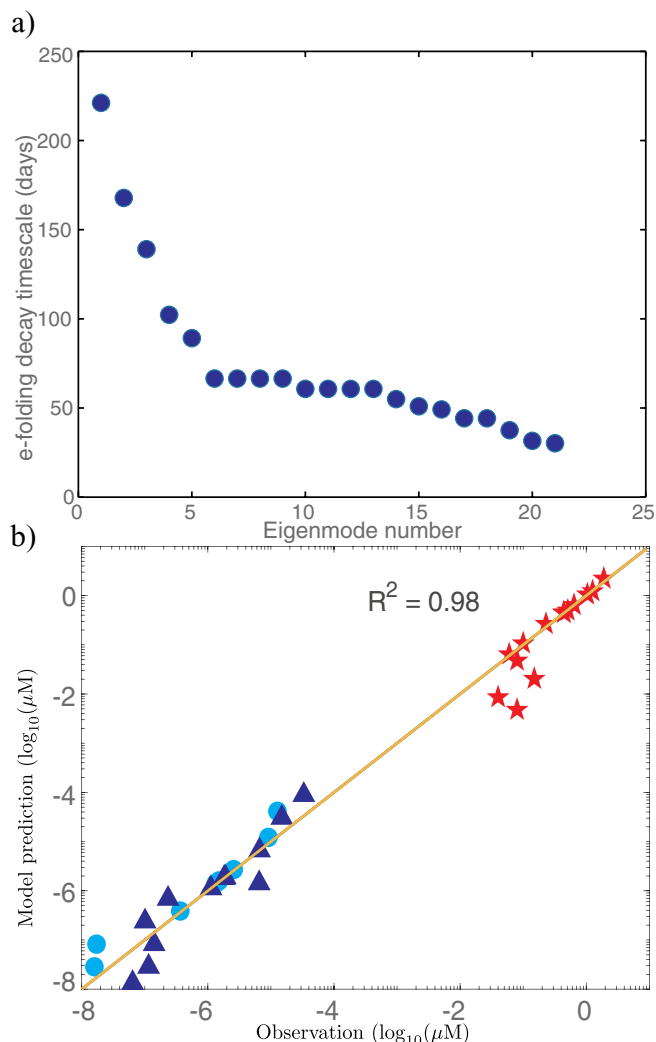
a)

b)

Fig. 3. a) Plot of e-folding decay timescale in units of days of slowly decaying eigenmodes (> 5 days) (second-order model). b) model versus observation comparisons for the second-order non steady-state model. Red stars represent POC, blue triangles correspond to pheopigments, and cyan circles stand for Chl *a*. (For interpretation of the references to colour in this figure legend, the reader is referred to the web version of this article.)

scaling the prior precision of these amplitudes. We note that in the limit $\Theta \to \infty$ we recover the steady state model. Whereas in the limit $\Theta \to 0$ the amplitudes are completely free to fit as much of the data variance as possible. To determine the value of Θ we maximized the corresponding evidence similar to Eq. 11 but now over the three-dimensional space spanned by Λ, Γ, and Θ. This analysis yielded a most probable value for the scaling of the prior precision on the weakly damped eigenmodes with $\log_{10}(\Theta) \sim 13$, a value that is so large as to effectively clamp the amplitudes to zero. This result suggests that conditioned on our limited dataset the steady-state model is more probable because it can fit the data reasonably well ($R^2 = 0.94$) with a much smaller number of free parameters than the model that retains the weakly damped dynamics. For reference we also fit the non-steady state model by prescribing $\log_{10}\Theta = -2$ and obtained an $R^2 = 0.98$ (Fig. 3b). By further reducing Θ we were able to capture up to 99% of the variance indicating that the residuals of the steady-state model project most strongly onto the model's weakly damped dynamics rather than on the neglected strongly damped dynamics, which we assumed a priori to be unimportant.

The optimal parameters calculated for both steady-state and non-steady-state models are listed in Table 2. The differences in the optimal parameter values are small compared to their uncertainties, which

indicates that the steady-state assumption is not a large source of bias in our model. A plot of the model-predicted concentrations against the observed concentrations is shown in Fig. 3b. The steady-state model ($R^2 = 0.94$) fits the data almost as well as the non steady-state case ($R^2 = 0.98$), but with significantly less parameters (13 for steady-state and 34 for non steady-state models). The optimal parameter estimates have strongly overlapping errorbars and are therefore consistent. The errorbars for the steady-state model are slightly smaller compared to those of the most-probable non steady-state model. Note that although the non-steady model with $\Theta = 0.01$ has the smallest parameter errorbars, we reject that model due to its very low probability (more than 10 orders of magnitude less probable). We thus report the parameter values from the steady-state model. Considering the large dynamic range of the data (up to 7 orders of magnitude), both models do a decent job of fitting the observational data.

3.3. Particle sinking velocity

In contrast to previous box models that assign an arbitrary sinking velocity for large particles (e.g. Clegg and Whitfield 1991; Murnane et al. 1990; Murnane 1994; Cochran et al. 1993; Cochran et al. 2000), in this study we built depth-dependent sinking velocity into the model by using a vertical flux transport operator **S**. Variable sinking velocities have been shown to better represent sinking particles in geochemical models (Kriest and Oschlies 2008). The power law model for the flux attenuation with depth, known as the Martin Curve, indicates either an increasing sinking speed or a decreasing remineralization rate with depth (Martin et al. 1987). Increasing sinking speed has also been suggested by analyses of sediment trap array data (Berelson 2002). On the other hand, when Xue and Armstrong (2009) applied the benchmark method to IRS time series sediment trap data collected at multiple locations, they obtained an average sinking speed of $220 \pm 65\,\mathrm{m\,d^{-1}}$, and concluded that particle sinking speed did not change with depth. Here we do not apply a constant sinking speed for three reasons.

First, results based on sediment trap data may not be applicable to the large-volume pump data. Traps are deployed for months, and are likely to capture a larger amount of fast-sinking particles. The relatively short sampling time that the pump is deployed decreases the chance of capturing really fast-sinking particles, which are rare in the ocean. According to Giering et al. (2016); Villa-Alfageme et al. (2014); Alonso-González et al. (2010), a large fraction of the particles sink at a speed lower than $40\,\mathrm{m\,d^{-1}}$. For comparison, we calculated particle sinking velocities based on an optimal '*b*' value and disaggregation rate constant (see Section 2.5). Large-size particle sinking velocity ranged from ~ 7 to $\sim 183\,\mathrm{m\,d^{-1}}$ with an average of $66.79 \pm 68.56\,\mathrm{m\,d^{-1}}$. Both the range and mean SV are similar to previous estimates for aggregates (e.g. Alldredge and Gotschalk 1988; Asper et al. 1992; Pilskaln et al. 1998), but lower than that for fecal pellets (Fowler and Small 1972; Komar et al. 1981). Small-size particle sinking velocity ranged from ~ 0.2 to $\sim 5\,\mathrm{m\,d^{-1}}$, with an average of $1.84 \pm 1.88\,\mathrm{m\,d^{-1}}$, much slower than that of large-size particles. The average sinking speed is slightly higher than the cutoff speed ($0.5\,\mathrm{m\,d^{-1}}$) estimated by Abramson et al. (2010) from Stokes' law.

Second, without a rate-determining factor like decay half-life in thorium models, we cannot simultaneously determine sinking speed and particle exchange rates. We tested our model by applying two different sinking speeds: $100\,\mathrm{m\,d^{-1}}$ and $200\,\mathrm{m\,d^{-1}}$. As shown in Table 3, disaggregation rate constants change proportionally with

Table 3
Parameter values of constant sinking speed model (unit: $\mathrm{yr^{-1}}$ except for sinking speed (SV) that is m $\mathrm{d^{-1}}$). Parameters are defined in Fig. 1.

SV	κ_1	κ_2	κ_3	α	β
$\omega = 100$	1.68	10.55	1.98	453	1096
$\omega = 200$	1.66	12.84	1.93	498	1722

sinking speed.

Lastly but most importantly, our objective here is to introduce a versatile method for calibrating parameters and to test the sensitivity of these inferences to different sampling methods (SV sediment traps versus large volume pumps) and to different tracers (thorium versus pigments). Since particle sinking velocities (SV) are rarely precisely measured, the arbitrary assignment (e.g., 100 or 200 m d^{-1}) of a sinking velocity could cause large uncertainties (Table 3). Our method does not require a value for SV, because the Martin Curve exponential *b* is an estimated parameter.

3.4. Particle exchange rate constants

The inverse model described here predicts a small-particle POC remineralization rate constant of $2.44^{+1.69}_{-1.00}$ yr^{-1} (0.41 yr), which is quite similar to the previous estimate ($1.5^{+0.5}_{-0.4}$ yr^{-1}) for slow-sinking particles) using SV sediment trap data from this site (Wang et al. 2017). It is also consistent to estimates in other oceanic regions at a corresponding depth range (1.6–2.4 yr^{-1}) (Clegg et al. 1991; Clegg and Whitfield 1991). However, the POC dissolution rate constants estimated here are significantly lower than those ($\sim$29–73 yr^{-1}) reported by Iversen and Ploug (2010), who determined the POC dissolution rate for freshly formed aggregates. The difference between our findings is most likely because they were looking at fresh, labile POC, and we were looking at more refractory material from depth that had been subject to considerable decomposition due to its slow sinking rate.

Chl-*a* and pheopigment degradation rate constants compare well to our previous estimates from sediment traps (Wang et al. 2017). For example, our estimates from trap-collected pigments were $1.6^{+0.4}_{-0.3}$ yr^{-1} for Chl-*a* and 2.1 $^{+0.7}_{-0.5}$yr^{-1} for pheopigment degradation rate constants. Our new corresponding estimates based on chloropigments collected using large-volume pumps are $1.68^{+1.74}_{-0.86}$ yr^{-1} and 2.06 $^{+1.86}_{-0.98}$ yr^{-1}, respectively.

The aggregation and disaggregation rate constants calculated here using pump chloropigment data are $2.78^{+2.01}_{-1.17}$ µM^{-1} yr^{-1} and $85.6^{+63.4}_{-36.4}$ yr^{-1}, respectively, assuming second-order reaction kinetics for aggregation. Using first-order kinetics, these rate constants are $3.18^{+3.05}_{-1.56}$ and $73.1^{+69.6}_{-35.6}$ yr^{-1}. Compared to estimates using SV sediment trap thorium data, these rate constants are much more similar to those estimated from SV sediment trap chloropigment data (3.20 and 149.9 yr^{-1}) under the same first-order aggregation and steady state assumptions (Table 2). Disaggregation rate constants from both pump and trap studies fall within the range of previous thorium-based estimates (0.8–6500 yr^{-1})) (e.g. Clegg and Whitfield 1991; Murnane et al. 1996; Lerner et al. 2016). Aggregation rate constants are also in agreement with previous thorium-based estimates. For example, Cochran et al. (1993) obtained a range of 1.1–33 yr^{-1} for an aggregation rate constant in the North Atlantic, and Nozaki et al. (1987) estimated aggregation rate constants in the Western Pacific as 2.36–12.3 yr^{-1} with large error bars.

In addition, we can calculate aggregation and disaggregation rates based on the most probable rate constants and particle concentrations. At the time of sampling, depth-averaged aggregation and disaggregation rates (2.91 and 9.04 µM yr^{-1}, respectively) are $\sim$1.3 to $\sim$4.2 times higher than dissolution of small-particle POC. Chl *a* and pheopigments have low aggregation rates because their extremely low concentrations give them little chance to collide and then aggregate. Disaggregation becomes the dominant process. This conclusion is mostly consistent with the idea that small and large particles exchange particle components via aggregation and disaggregation during low flux times, because we found that disaggregation is the dominant process for all tracers, while the importance of aggregation depends on tracer concentration, which determines the probability to collide. Abramson et al. (2010) have previously suggested this based on a simple, but non-quantitative, comparison of the chloropigment composition of traps and pumps at the Medflux site in both 2003 and 2005. They suggested that

aggregation and disaggregation were low during high flux times, and high during low flux times.

It is interesting to compare results obtained in this study using chloropigment tracers and in-situ pumps, with those obtained using the same chloropigment tracers but sampled using SV sediment traps, and with those obtained using SV sediment trap thorium data. These rate constants are summarized in Table 2. Note that the data used in the three studies were sampled at the same location and roughly the same time (sediment traps had a longer deployment time). The comparison shows that aggregation/disaggregation rate constants are similar when the same tracers are used, even though the sampling methods are different. Aggregation/disaggregation rate constants are significantly different when different tracers are used, even when the tracers were sampled using the same method. These comparisons are intriguing because they suggest that parameters estimated using the same tracers but different sampling techniques are more consistent than those using the same techniques but different tracers. Chloropigments, as integral parts of particulate organic matter, may more accurately trace the particle dynamics than thorium isotopes because the later tracer is also influenced by adsorption and desorption processes (especially when ^{234}Th is used), which might obscure the underlying particle exchange processes.

4. Conclusions

In this study, we applied both steady-state and non steady-state Bayesian inverse methods to chloropigment data obtained using large volume pumps at the MedFlux site in the Mediterranean Sea. We also compared both first- and second-order reaction kinetics for aggregation. The samples used were collected during a low flux period well after the normal spring bloom. Particles appeared to have experienced extensive aggregation and disaggregation. The order of reaction kinetics did not significantly influence the estimated rate constants, however, the second-order model fits the data better, in agreement with the idea that second-order reaction kinetics for aggregation is a better model of the particle dynamics. Comparison to previous results estimated using thorium and pigment data but sampled using sediment traps indicate that the two different sampling and model methods have less influence on particle aggregation and disaggregation rate constant estimations than do the two different tracers themselves. The comparison also highlights the different characteristics between pigment tracers and thorium tracers that we have discussed previously. Future work should build a combined model based on multiple tracers that are simultaneously collected using either large volume pumps or SV sediment traps since the results are not overly sensitive to the sampling methods.

Code availability

The code is available at https://doi.org/10.5281/zenodo.2595433.

References

Abramson, L., Lee, C., Liu, Z., Wakeham, S.G., Szlosek, J., 2010. Exchange between suspended and sinking particles in the Northwest Mediterranean as inferred from the organic composition of in situ pump and sediment trap samples. Limnol. Oceanogr. 55 (2), 725–739.

Alldredge, A.L., Gotschalk, C., 1988. In situ settling behavior of marine snow. Limnol. Oceanogr. 33 (3), 339–351.

Alonso-González, I.J., Arstegui, J., Lee, C., Sanchez-Vidal, A., Calafat, A., Fabrés, J., Sangrá, P., Masqué, P., Hernández-Guerra, A., Bentez-Barrios, V., 2010. Role of slowly settling particles in the ocean carbon cycle. Geophys. Res. Lett. 37 (13).

Armstrong, R.A., Lee, C., Hedges, J.I., Honjo, S., Wakeham, S.G., 2002. A new, mechanistic model for organic carbon fluxes in the ocean based on the quantitative association of POC with ballast minerals. Deep-Sea Res. II 49 (1–3), 219–236.

Armstrong, R.A., Peterson, M.L., Lee, C., Wakeham, S.G., 2009. Settling velocity spectra and the ballast ratio hypothesis. Deep-Sea Res. II 56 (18), 1470–1478.

Asper, V.L., Honjo, S., Orsi, T.H., 1992. Distribution and transport of marine snow aggregates in the Panama basin. Deep-Sea Res. Part A. Oceanographic Research Papers 39 (6), 939–952.

Bacon, M.P., Anderson, R.F., 1982. Distribution of thorium isotopes between dissolved and particulate forms in the deep sea. J. of Geophys. Res.: Oceans 87 (C3), 2045–2056.

Berelson, W.M., 2002. Particle settling rates increase with depth in the ocean. Deep-Sea Res. II 49 (1–3), 237–251.

Bishop, J.K., Lam, P.J., Wood, T.J., 2012. Getting good particles: accurate sampling of particles by large volume in-situ filtration. Limnol. Oceanogr. Methods 10 (9), 681–710.

Clegg, S.L., Whitfield, M., 1991. A generalized model for the scavenging of trace metals in the open ocean-II. Thorium scavenging. Deep-Sea Res. I 38 (1), 91–120.

Clegg, S.L., Bacon, M.P., Whitfield, M., 1991. Application of a generalized scavenging model to thorium isotope and particle data at equatorial and high-latitude sites in the Pacific Ocean. J. Geophys. Res. 96 (C11), 20655–20670.

Cochran, J., Masqué, P., 2003. Short-lived U/Th series radionuclides in the ocean: tracers for scavenging rates, export fluxes and particle dynamics. Rev. Mineral. Geochem. 52 (1), 461–492.

Cochran, J., Buesseler, K.O., Bacon, M.P., Livingston, H.D., 1993. Thorium isotopes as indicators of particle dynamics in the upper ocean: results from the JGOFS North Atlantic bloom experiment. Deep-Sea Res. I 40 (8), 1569–1595.

Cochran, J., Buesseler, K.O., Bacon, M.P., Wang, H.W., Hirschberg, D.J., Ball, L., Andrews, J., Crossin, G., Fleer, A., 2000. Short-lived thorium isotopes (^{234}Th, ^{228}Th) as indicators of POC export and particle cycling in the Ross Sea, Southern Ocean. Deep-Sea Res. II 47 (15–16), 3451–3490.

Cochran, J.K., Miquel, J.C., Armstrong, R., Fowler, S.W., Masqué, P., Gasser, B., Hirschberg, D., Szlosek, J., Rodriguez, Y., Baena, A.M.R., Verdeny, E., Stewart, G., 2009. Time-series measurements of ^{234}Th in water column and sediment trap samples from the northwestern Mediterranean Sea. Deep-Sea Res. II 56 (18), 1487–1501.

D'Ortenzio, F., Iudicone, D., de Boyer Montegut, C., Testor, P., Antoine, D., Marullo, S., Santoleri, R., Madec, G., 2005. Seasonal variability of the mixed layer depth in the Mediterranean Sea as derived from in situ profiles. Geophys. Res. Lett. 32 (12), L12605.

Emerson, S., 2014. Annual net community production and the biological carbon flux in the ocean. Glob. Biogeochem. Cycles 28 (1), 14–28.

Fowler, S.W., Small, L.F., 1972. Sinking rates of euphausiid fecal pellets. Limnol. Oceanogr. 17 (2), 293–296.

Giering, S., Sanders, R., Martin, A., Lindemann, C., Möller, K., Daniels, C., Mayor, D., St. John, M., 2016. High export via small particles before the onset of the North Atlantic spring bloom. J. of Geophys. Res. Oceans 121 (9), 6929–6945.

Houpert, L., Testor, P., de Madron, X.D., Somot, S., Dortenzio, F., Estournel, C., Lavigne, H., 2015. Seasonal cycle of the mixed layer, the seasonal thermocline and the upper-ocean heat storage rate in the mediterranean sea derived from observations. Prog. in Oceanogr., vol. 132, 333–352.

Iversen, M., Ploug, H., 2010. Ballast minerals and the sinking carbon flux in the ocean: carbon-specific respiration rates and sinking velocity of marine snow aggregates. Biogeosciences 7, 2613–2624.

Jackson, G.A., 1990. A model of the formation of marine algal flocs by physical coagulation processes. Deep-Sea Res. I 37 (8), 1197–1211.

Jackson, G.A., Burd, A.B., 2015. Simulating aggregate dynamics in ocean biogeochemical models. Prog. Oceanogr. 133, 55–65.

Komar, P.D., Morse, A.P., Small, L.F., Fowler, S.W., 1981. An analysis of sinking rates of natural copepod and euphausiid fecal pellets. Limnol. Oceanogr. 26 (1), 172–180.

Kriest, I., Oschlies, A., 2008. On the treatment of particulate organic matter sinking in large-scale models of marine biogeochemical cycles. Biogeosciences 5 (1), 55–72.

Lee, C., Wakeham, S.G., 1988. Organic matter in seawater: Biogeochemical processes. In: Riley, J.P. (Ed.), Chemical Oceanography. Vol. 9. Academic Press.

Lee, C., Armstrong, R.A., Cochran, J.K., Engel, A., Fowler, S.W., Goutx, M., Masqué, P., Miquel, J.C., Peterson, M., Tamburini, C., Wakeham, S.G., 2009a. A. MedFlux: investigations of particle flux in the twilight zone. Deep-Sea Res. II 56 (18), 1363–1368.

Lee, C., Peterson, M.L., Wakeham, S.G., Armstrong, R.A., Cochran, J.K., Miquel, J.C., Fowler, S.W., Hirschberg, D., Beck, A., Xue, J., 2009b. Particulate organic matter and ballast fluxes measured using time-series and settling velocity sediment traps in the northwestern Mediterranean Sea. Deep-Sea Res. II 56 (18), 1420–1436.

Lerner, P., Marchal, O., Lam, P.J., Anderson, R.F., Buesseler, K., Charette, M.A., Edwards, R.L., Hayes, C.T., Huang, K.F., Lu, Y., Robinson, L.F., Solow, A., 2016. Testing models of thorium and particle cycling in the ocean using data from station GT11-22 of the U.S. GEOTRACES North Atlantic section. Deep-Sea Res. I 113, 57–79.

Lima, I.D., Lam, P.J., Doney, S.C., 2014. Dynamics of particulate organic carbon flux in a global ocean model. Biogeosciences 11 (4), 1177–1198.

MacKay, D.J.C., 1992. Bayesian interpolation. Neural Comput. 4, 415–447.

Marchal, O., Lam, P.J., 2012. What can paired measurements of Th isotope activity and particle concentration tell us about particle cycling in the ocean? Geochim. Cosmochim. Acta 90, 126–148.

Martin, J., Knauer, G., Karl, D., Broenkow, W., 1987. VERTEX: carbon cycling in the Northeast Pacific. Deep-Sea Res. 34, 267–285.

Marty, J.C., Chiavérini, J., Pizay, M.D., Avril, B., 2002. Seasonal and interannual dynamics of nutrients and phytoplankton pigments in the western Mediterranean Sea at the DYFAMED time-series station (1991-1999). Deep-Sea Res. II 49 (11), 1965–1985.

McCave, I.N., 1975. Vertical flux of particles in the ocean. Deep-Sea Res. I 22 (7), 491–502.

McDonnell, A.M.P., Buesseler, K.O., 2010. Variability in the average sinking velocity of marine particles. Limnol. Oceanogr. 55 (5), 2085–2096.

Murnane, R.J., 1994. Determination of thorium and particulate matter cycling parameters at station P: a reanalysis and comparison of least squares techniques. J. Geophys. Res. 99 (C2), 3393–3405.

Murnane, R.J., Sarmiento, J.L., Bacon, M.P., 1990. Thorium isotopes, particle cycling models, and inverse calculations of model rate constants. J. Geophys. Res. 95 (C9), 16195.

Murnane, R.J., Cochran, J.K., Buesseler, K.O., Bacon, M.P., 1996. Least-squares estimates of thorium, particle, and nutrient cycling rate constants from the JGOFS North Atlantic bloom experiment. Deep-Sea Res. I 43 (2), 239–258.

Nozaki, Y., Yang, H.-S., Yamada, M., 1987. Scavenging of thorium in the ocean. J. Geophys. Res. 92 (C1), 772.

Peterson, M.L., Wakeham, S.G., Lee, C., Askea, M.A., Miquel, J.C., 2005. Novel techniques for collection of sinking particles in the ocean and determining their settling rates. Limnol. Oceanogr. Methods 3, 520–532.

Peterson, M.L., Fabres, J., Wakeham, S.G., Lee, C., Alonso, I.J., Miquel, J.C., 2009. Sampling the vertical particle flux in the upper water column using a large diameter free-drifting NetTrap adapted to an indented rotating sphere sediment trap. Deep-Sea Res. II 56 (18), 1547–1557.

Pilskaln, C.H., Lehmann, C., Paduan, J.B., Silver, M.W., 1998. Spatial and temporal dynamics in marine aggregate abundance, sinking rate and flux: Monterey Bay, Central California. Deep-Sea Res. II 45 (8–9), 1803–1837.

Roy-Barman, M., Jeandel, C., Souhaut, M., van der Loeff, M.R., Voege, I., Leblond, N., Freydier, R., 2005. The influence of particle composition on thorium scavenging in the NE Atlantic Ocean (POMME experiment). Earth Planet. Sci. Lett. 240 (3–4), 681–693.

Savoye, N., Benitez-Nelson, C., Burd, A.B., Cochran, J.K., Charette, M., Buesseler, K.O., Jackson, G.A., Roy-Barman, M., Schmidt, S., Elskens, M., 2006. ^{234}Th sorption and export models in the water column: A review. Mar. Chem. 100 (3–4 SPEC. ISS), 234–249.

Teng, Y.-C., Primeau, F.W., Moore, J.K., Lomas, M.W., Martiny, A.C., 2014. Global-scale variations of the ratios of carbon to phosphorus in exported marine organic matter. Nat. Geosci. 7 (12), 895–898.

Villa-Alfageme, M., De Soto, F., Le Moigne, F.A., Giering, S., Sanders, R., Garca-Tenorio, R., 2014. Observations and modeling of slow-sinking particles in the twilight zone. Glob. Biogeochem. Cycles 28 (11), 1327–1342.

Wang, W.-L., Armstrong, R.A., Cochran, J.K., Heilbrun, C., 2016. ^{230}Th and ^{234}Th as coupled tracers of particle cycling in the ocean: a maximum likelihood approach. Deep Sea Res. I 111, 61–70.

Wang, W.-L., Lee, C., Cochran, J.K., Primeau, F.W., Armstrong, R.A., 2017. A novel statistical analysis of chloropigment fluxes to constrain particle exchange and organic matter remineralization rate constants in the Mediterranean Sea. Mar. Chem. 192, 49–59.

Wang, W.-L., Moore, J., Martiny, A., Primeau, F., 2019. Convergent estimates of marine nitrogen fixation. Nature 566 (7743), 205.

Xue, J., Armstrong, R.A., 2009. An improved benchmark method for estimating particle settling velocities from time-series sediment trap fluxes. Deep-Sea Res. II 56 (18), 1479–1486.